

THE EXTENDED FE DISTRIBUTION IN THE INTRACLUSTER MEDIUM AND THE IMPLICATIONS REGARDING AGN HEATING.

LAURENCE P. DAVID & PAUL E.J. NULSEN
 Harvard-Smithsonian Center for Astrophysics, 60 Garden St., Cambridge, MA 02138;
 david@cfa.harvard.edu
accepted for publication in The Astrophysical Journal

ABSTRACT

We present a systematic analysis of XMM-Newton observations of 8 cool-core clusters of galaxies and determine the Fe distribution in the intracluster medium relative to the stellar distribution in the central dominant galaxy (CDG). Our analysis shows that the Fe is significantly more extended than the stellar mass in the CDG in all of the clusters in our sample, with a slight trend of increasing extent with increasing central cooling time. The excess Fe within the central 100 kpc in these clusters can be produced by Type Ia supernovae from the CDG over the past 3-7 Gyr. Since the excess Fe primarily originates from the CDG, it is a useful probe for determining the motion of the gas and the mechanical energy deposited by AGN outbursts over the past ~ 5 Gyr in the centers of clusters. We explore two possible mechanisms for producing the greater extent of the Fe relative to the stars in the CDG, including: bulk expansion of the gas and turbulent diffusion of Fe. Assuming the gas and Fe expand together, we find that a total energy of $10^{60} - 10^{61}$ erg s⁻¹ must have been deposited into the central 100 kpc of these clusters to produce the presently observed Fe distributions. Since the required enrichment time for the excess Fe is approximately 5 Gyr in these clusters, this gives an average AGN mechanical power over this time of $10^{43} - 10^{44}$ erg s⁻¹. The extended Fe distribution in cluster cores can also arise from turbulent diffusion. Assuming steady-state (i.e., the outward mass flux of Fe across a given surface is equal to the mass injection rate of Fe within that surface) we find that diffusion coefficients of $10^{29} - 10^{30}$ cm² s⁻¹ are required to maintain the presently observed Fe profiles. We find that heating by both turbulent diffusion of entropy and dissipation are important heating mechanisms in cluster cores. In half of the clusters with central cooling times greater than 1 Gyr, we find that heating by turbulent diffusion of entropy alone can balance radiative losses. In the remaining clusters, some additional heating by turbulent dissipation, with turbulent velocities of 150 - 300 km s⁻¹, is required to balance radiative cooling. We also find that the average Type Ia supernova fraction within the central 100 kpc of these clusters is 0.53 (roughly twice the solar value) based on the Si-to-Fe mass ratio. This implies a total (Type Ia plus core collapse) supernova heating rate less than 10% of the bolometric X-ray luminosity within the centers of clusters.

Subject headings: galaxies:clusters:general – cooling flows – galaxies:abundances – intergalactic medium – galaxies:active – X-rays:galaxies:clusters

1. INTRODUCTION

There is compelling evidence from Chandra observations that heating by a central AGN has a dramatic impact on the energetics of the hot gas in early-type galaxies, groups, and clusters of galaxies (McNamara & Nulsen 2007; McNamara et al. 2000, Finoguenov & Jones 2002; Churazov et al. 2002; Fabian et al. 2003, Blanton et al. 2003, Mazzotta, Edge & Markevitch 2003; Kraft et al. 2003; Nulsen et al. 2005a, 2005b; Forman et al. 2005, Wise et al. 2007). Heating from AGN driven shocks and buoyantly rising bubbles filled with radio emitting plasma will also affect the distribution of the hot gas and heavy elements in the central regions of clusters. Einstein and Rosat observations showed that the hot gas in groups is more extended (compared to the dark matter) than the gas in rich clusters (David, Jones & Forman 1995; Jones & Forman 1999). The variable extent of the hot gas relative to the dark matter breaks the self-similarity between groups and rich clusters. The origin of this self-similarity breaking has usually been attributed to some form of non-gravitational heating or “pre-heating” (David, Jones & Forman 1995; Lloyd-Davies, Ponman & Cannon 2000). Recent estimates on the AGN mechanical heating rate, or “cavity power”, in cool-core clusters (Birzan et al. 2004; Best et al. 2006; Rafferty et al. 2006; Dunn & Fabian 2008) and the large radius of the shock in Hydra A (Nulsen et al. 2005a) suggest that much of the pre-heating required to break the self-similarity of clusters could arise dur-

ing the formation and subsequent growth of supermassive black holes in the host galaxies in clusters.

Observations by ASCA, BeppoSAX, XMM-Newton, and Chandra have shown that clusters with cool cores have Fe abundance profiles that increase toward the cluster center, while non cool-core clusters (which have probably experienced a recent merger) have flatter Fe abundance profiles (Finoguenov, David & Ponman 2000; Fukazawa et al. 2000; De Grandi et al. 2004; Tamura et al. 2004; Vikhlinin et al. 2005; Baldi et al. 2007). Discussions about the history of chemical enrichment in clusters of galaxies can be found in Renzini et al. (1993), Loewenstein (2006), and Matteucci (2007). The Fe is a good tracer for determining the past motion of the gas in the central region of clusters since it primarily originates from Type Ia supernovae (SNe Ia) from the CDG (Finoguenov et al. 2000; Finoguenov et al. 2001; Bohringer et al. 2004; De Grandi et al. 2004). Most studies have found that the Fe is more extended than the light of the CDG (David et al. 2001; Rebusco et al. 2005, 2006). The greater extent of the Fe compared to the light of the CDG is likely the result of AGN mechanical heating. Tornatore et al. (2004) presented a series of numerical simulations that tracked the chemical enrichment of the gas in clusters and concluded that without any AGN feedback, the resulting Fe abundance profiles are more centrally concentrated than those observed.

We present in this paper a systematic analysis of 8 relaxed, cool-core clusters with measured optical surface brightness profiles for their CDG and make a direct comparison between the

TABLE 1
GENERAL CLUSTER PROPERTIES

| Name | z | kT (keV) | $L_R(r < 100\text{kpc})$ ($L_{\odot R}$) | $L_{bol}(r < 100\text{kpc})$ (erg s^{-1}) | $t_c(r = 10\text{kpc})$ (yr) |
|-------|--------|-------------|---|---|---------------------------------|
| A262 | 0.0163 | 2.04 | 1.67×10^{11} | 1.96×10^{43} | 7.5×10^8 |
| A496 | 0.0329 | 3.23 | 4.44×10^{11} | 1.29×10^{44} | 6.0×10^8 |
| A2199 | 0.0301 | 3.77 | 4.12×10^{11} | 1.52×10^{44} | 6.8×10^8 |
| A2589 | 0.0414 | 3.39 | 2.81×10^{11} | 4.85×10^{43} | 2.3×10^9 |
| A3558 | 0.048 | 5.08 | 7.47×10^{11} | 1.03×10^{44} | 1.9×10^9 |
| A3571 | 0.0391 | 6.39 | 8.50×10^{11} | 1.85×10^{44} | 1.8×10^9 |
| A3581 | 0.023 | 1.62 | 1.72×10^{11} | 2.78×10^{43} | 6.6×10^8 |
| A4059 | 0.0475 | 3.47 | 5.13×10^{11} | 9.31×10^{43} | 1.1×10^9 |

Notes: Cluster name, redshift, emission-weighted temperature within 100 kpc, R-band luminosity of the central dominant galaxy within 100 kpc, bolometric X-ray luminosity within 100 kpc and isobaric radiative cooling time at 10 kpc from the cluster center.

Fe and stellar mass density distributions. We find that the total Fe and the central Fe excess are significantly more extended than the stars in the CDG in all of the clusters in our sample. We investigate two possible origins for the greater extent of the Fe relative to the stars: 1) bulk expansion of the gas due to AGN heating and 2) outward diffusion of Fe due to turbulent gas motions.

This paper is organized in the following manner. In § 2, we present our cluster sample and in § 3 we discuss the details of our XMM-Newton data reduction. The total Fe mass, Si mass, SNe Ia fraction, total supernova heating rate and the distribution of the excess Fe relative to the stars in the CDG are presented in section § 4. In § 5, we explore potential mechanisms for producing the more extended Fe distribution, including: bulk expansion of the gas due to AGN heating and turbulent diffusion of Fe. The implications of our findings regarding the AGN cooling flow feedback mechanism are discussed in § 6.

2. CLUSTER SAMPLE

We searched the XMM-Newton archive for deep observations of clusters that have CDGs with optical surface brightness profiles measured by Graham et al. (1996). We excluded clusters with significant substructure and redshifts greater than $z = 0.05$ to ensure adequate spatial resolution of the Fe distribution. Our final sample of 8 clusters is listed in Table 1. We use XMM-Newton data in our study since good photon statistics are required to accurately determine the Fe distribution. The Fe abundance in these clusters typically decreases by a factor of 2 over scales of $3 - 5'$, so the $30''$ resolution of the XMM-Newton EPIC cameras for spectroscopic imaging is sufficient for determining the Fe distribution in these clusters. The photon statistics in most of the Chandra observations of these clusters are insufficient to constrain the Fe distribution on smaller angular scales.

Graham et al. (1996) fit both Sersic and de Vaucouleurs profiles to the R-band images of the CDGs in our sample and found that most of the CDGs are better modeled with Sersic profiles, except for the CDGs in A262 and A3581, which are adequately fit with de Vaucouleurs profiles. By fitting the 2-D images of a sample of 24 higher redshift CDGs, Gonzalez, Zabludoff & Zaritsky (2005) found that the sum of two de Vaucouleurs profiles is a better representation of the surface brightness profile compared to a single Sersic model. However, their Fig. 3 shows that the azimuthally averaged surface brightness profiles are

equally well represented by either a Sersic model or the sum of two de Vaucouleurs models. Thus, the use of a Sersic model for computing azimuthally averaged quantities should be sufficient. Graham et al. list the effective radii for the CDGs in kpc based on the distance indicator in Lauer & Postman (1994). We adjust these radii using $H_0 = 70 \text{ km s}^{-1} \text{ Mpc}^{-1}$, $\Omega_M = 0.3$ and $\Omega_\Lambda = 0.7$, which is the standard cosmology adopted throughout this paper. We correct the surface brightness at the effective radius listed in Graham et al. for extinction and apply a K-correction. The extinction values are obtained from Schlegel et al. (1998) and the K-correction, appropriate for an early-type galaxy, is obtained from Postman & Lauer (1995). The stellar mass density profiles for the CDGs are then derived from the Sersic profiles for all the CDGs except those in A262 and A3581, for which we use the de Vaucouleurs profiles, using Abel's formula (Binney & Tremaine 1987) and $M_*/L_R = 3.5 M_\odot/L_{\odot R}$ (which is based on the average optical colors of the CDGs in our sample and the stellar synthesis models of Bell & de Jong 2001).

3. XMM-NEWTON DATA REDUCTION

All archived XMM-Newton data were reprocessed using the `emchain` and `epchain` tasks in SASS v7.0 with the standard flag settings. To screen for background flares, we extracted light curves from each detector in the 8-12 keV band within an annulus $10 - 12'$ from the cluster centers. Time intervals with 8-12 keV count rates more the 3σ above the mean count rate were excised from further analysis. Background data sets were generated using the procedures outlined in Arnaud et al. (2002) using the blank field background data sets from Read & Ponman (2003) and the filter-closed charged particle background data sets from Marty et al. (2003).

After excising the emission from all detected point sources, a background subtracted, exposure corrected 0.5-7.0 keV surface brightness profile was generated for each cluster by combining the data from all 3 EPIC cameras using the optical centroid of the CDG as the origin. Based on the cumulative number of net 0.5-7.0 keV counts, we generated three sets of concentric annular regions that enclose at least 10000, 20000 and 40000 net counts with a minimum width for each annulus of $30''$. For each cluster, source spectra were extracted from all 3 EPIC detectors in the three sets of annular regions along with background spectra from the same regions in the background data sets. Photon weighted response and effective area files were generated for

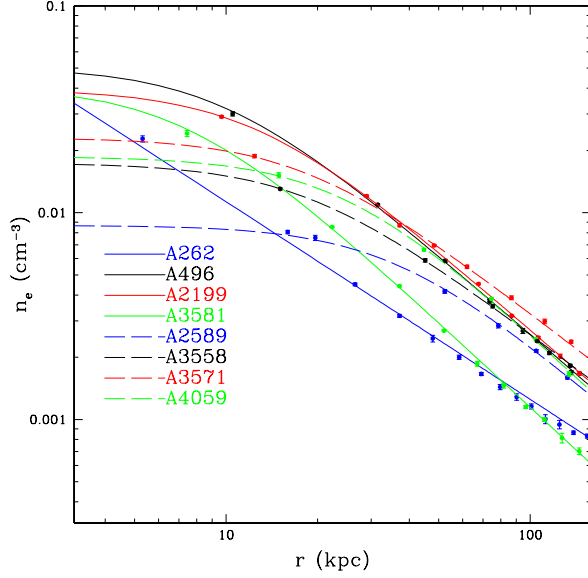


FIG. 1.— Electron number density vs. radius for each cluster in our sample. Clusters with cooling times at 10 kpc less than 1 Gyr are shown with solid lines and clusters with longer cooling times are shown with dashed lines.

each spectrum using the SAS tasks `rmfgen` and `arfgen`. The three sets of spectra for each cluster were then deprojected assuming spherical symmetry. The spectra were fit to a single temperature `vapex` model in the 0.8–8.0 keV bandpass with the hydrogen column density frozen at the galactic value. The abundances of all α processed elements along with the Fe abundance and temperature were treated as free parameters. The Ni abundance was linked to the Fe abundance. All abundances are measured relative to the solar values in Grevesse & Sauval (1998). The gas density profile for each cluster is determined from the deprojected emission measures of the set of spectra with at least 10,000 net counts. The temperature and Fe abundance profiles are based on the deprojected values from the set of spectra with at least 20,000 net counts. The Si abundance profiles are derived from the deprojected values from the set of spectra with at least 40,000 net counts. We also extracted a single spectrum from the inner 100 kpc of each cluster to determine the emission-weighted temperature and bolometric X-ray luminosity within this region (see Table 1).

4. THE TOTAL AND EXCESS FE MASS WITHIN THE CENTRAL 100 KPC

The general, azimuthally-averaged de-projected properties (density, temperature, entropy, and Fe abundance profiles) of the clusters in our sample are shown in Figs. 1–4. We divide the clusters into two sub-samples based on the cooling time of the hot gas at a radial distance of 10 kpc from the CDG (see Table 1). Clusters with cooling times less than 1 Gyr are plotted with solid lines while clusters with longer cooling times are plotted with dashed lines. The deprojected density profiles were fitted to a single β model and the best-fit models are shown in Fig. 1. The deprojected temperature profiles were fitted with the analytic function used by Allen, Schmidt & Fabian (2001) and the resulting profiles are shown in Fig. 2. For the Fe abundance profiles shown in Fig. 3, we fitted the data to a single β model plus a constant. These figures show that the general cluster properties can be characterized by their central cooling

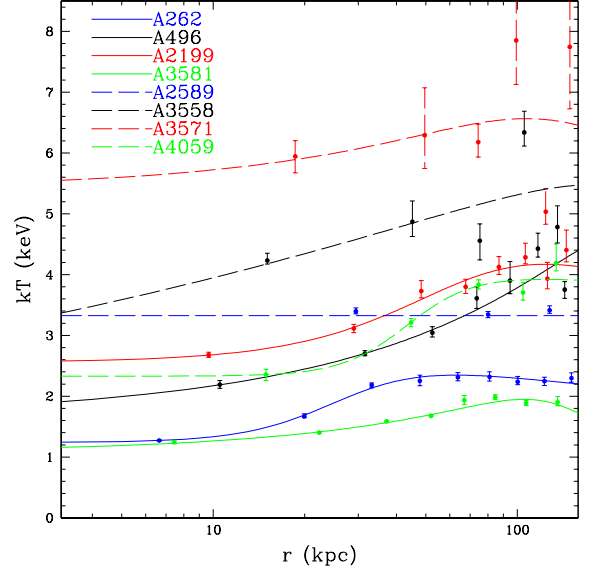


FIG. 2.— Deprojected temperature vs. radius for each cluster in our sample. The line types are described in the caption to Fig. 1.

time. Clusters with short cooling times have the highest central densities and lowest central entropies. While all the clusters, except A2589, have a positive temperature gradient at small radii, the relative temperature decrement is greater in clusters with shorter cooling times. To determine the total gas mass, Fe mass and Si mass within the central 100 kpc in these clusters, we generated 1000 realizations of the cumulative masses based on the best fit values of the gas density, Fe abundance and Si abundance at each radius, along with their associated 1σ uncertainties. From these 1000 realizations we determined the mean cumulative mass at each radius along with the 1σ uncertainty. The excess Fe mass within the central 100 kpc is calculated assuming that all clusters have a uniform Fe abundance of 0.3 solar at large radii, which is consistent with observations from ASCA, BeppoSax, XMM-Newton and Chandra

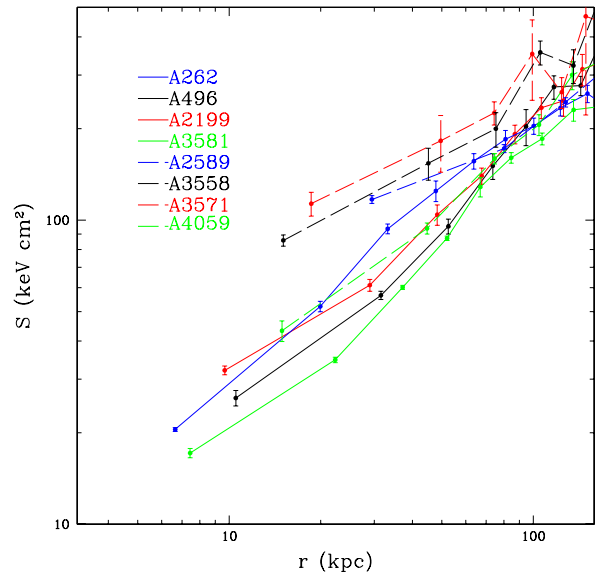


FIG. 3.— Entropy vs. radius for each cluster in our sample. The line types are described in the caption to Fig. 1.

TABLE 2
GAS MASS AND FE MASS WITHIN THE CENTRAL 100 KPC

| Name | M_{gas} (M_{\odot}) | $M_{\text{Fe}}(\text{tot})$ (M_{\odot}) | $M_{\text{Fe}}(\text{ex})$ (M_{\odot}) | $f_{\text{Fe}}(\text{ex})$ | $M_{\text{Fe}}(\text{tot})/L_R$ | $M_{\text{Fe}}(\text{ex})/L_R$ |
|-------|-------------------------------------|--|---|----------------------------|---------------------------------|--------------------------------|
| A262 | 2.1×10^{11} | $(2.1 \pm 0.2) \times 10^8$ | $(1.3 \pm 0.1) \times 10^8$ | 0.62 | 1.3×10^{-3} | 7.8×10^{-4} |
| A496 | 5.1×10^{11} | $(5.6 \pm 0.8) \times 10^8$ | $(3.6 \pm 0.5) \times 10^8$ | 0.64 | 1.3×10^{-3} | 8.1×10^{-4} |
| A2199 | 5.4×10^{11} | $(4.8 \pm 0.5) \times 10^8$ | $(2.7 \pm 0.3) \times 10^8$ | 0.56 | 1.2×10^{-3} | 6.6×10^{-4} |
| A2589 | 3.8×10^{11} | $(4.2 \pm 0.3) \times 10^8$ | $(2.8 \pm 0.2) \times 10^8$ | 0.67 | 1.5×10^{-3} | 9.9×10^{-4} |
| A3558 | 4.6×10^{11} | $(4.3 \pm 0.9) \times 10^8$ | $(2.5 \pm 0.5) \times 10^8$ | 0.58 | 5.7×10^{-4} | 3.3×10^{-4} |
| A3571 | 5.8×10^{11} | $(4.8 \pm 0.1) \times 10^8$ | $(2.6 \pm 0.5) \times 10^8$ | 0.54 | 5.5×10^{-4} | 3.0×10^{-4} |
| A3581 | 2.4×10^{11} | $(2.2 \pm 0.1) \times 10^8$ | $(1.3 \pm 0.08) \times 10^8$ | 0.59 | 1.3×10^{-3} | 7.6×10^{-4} |
| A4059 | 5.0×10^{11} | $(6.4 \pm 0.6) \times 10^8$ | $(4.5 \pm 0.5) \times 10^8$ | 0.70 | 1.2×10^{-3} | 8.8×10^{-4} |

Notes: Cluster name, gas mass within 100 kpc, total Fe mass within 100 kpc, excess Fe mass within 100 kpc, ratio of the excess Fe mass to the total Fe mass, ratio of total Fe mass to L_R of the CDG and ratio of excess Fe mass to L_R of the CDG. All errors are given at the 1σ confidence level.

(e.g., Finoguenov, David & Ponman 2000; De Grandi et al. 2004; Tamura et al. 2004; Vikhlinin et al. 2005; Baldi et al. 2007). The resulting gas mass, total Fe mass, excess Fe mass, ratio of excess Fe mass to total Fe mass and the ratios of total and excess Fe mass to the R-band luminosity of the CDGs are shown in Table 2. The mean values of M_{Fe}/L_R and $M_{\text{Fe}}(\text{ex})/L_R$ within the central 100 kpc in our sample are $9.0 \times 10^{-4} M_{\odot}/L_R$ and $6.9 \times 10^{-4} M_{\odot}/L_R$, respectively. Using an average B-R=1.8 for the CDGs in our sample (from the photometric tables in NED), gives mean values of M_{Fe}/L_B and $M_{\text{Fe}}(\text{ex})/L_B = 0.0015$ and $0.0012 M_{\odot}/L_B$. Our mean value of M_{Fe}/L_B within the central 100 kpc is consistent with the results in Finoguenov et al. (2000) derived from a sample of 11 relaxed clusters observed by ASCA.

The total Si mass within the central 100 kpc in these clusters is shown in Table 3 along with the total Si-to-Fe mass ratio relative to the solar value. In addition to the statistical errors shown for the Si mass, a systematic error of 10% should also be

included to account for cross-calibration issues between the EPIC cameras (de Plaa et al. 2007). All of the [Si/Fe] values in our cluster sample are subsolar, indicating a greater relative enrichment by SNe Ia. The mean value of [Si/Fe] for our cluster sample is -0.17. Adopting the yields for SNe Ia from the delayed detonation model (WDD2) of Iwamoto et al. (1999) ($y_{\text{SNeIa}}(\text{Fe}) = 0.713 M_{\odot}$ and $y_{\text{SNeIa}}(\text{Si}) = 0.206 M_{\odot}$) and the yields for core collapse supernovae (SNcc) from Tsujimoto et al. (1995) ($y_{\text{cc}}(\text{Fe}) = 0.084 M_{\odot}$ and $y_{\text{cc}}(\text{Si}) = 0.105 M_{\odot}$), the mean value of [Si/Fe] in our sample gives a SNe Ia fraction of $f_{\text{SNeIa}} = 0.53$. Tsujimoto et al. (1995) estimated that $N_{\text{SNeIa}}/N_{\text{cc}} = 0.15$ ($f_{\text{SNeIa}} = 0.17$) is required to reproduce the observed abundance pattern of 14 elements from oxygen to nickel in the Galaxy based on the SNe Ia yields from the W7 model of Thielemann, Nomoto & Hashimoto (1993), the same SNcc yields that we have adopted and the solar abundances in Anders & Grevesse (1989). Based on our adopted supernova yields and the solar abundances in Grevesse & Sauval (1998), $f_{\text{SNeIa}} = 0.23$ is required to reproduce the solar Si-to-Fe mass ratio.

Our estimates of f_{SNeIa} are roughly consistent with previous studies based on XMM-Newton observations of clusters. de Plaa et al. (2006) obtained $f_{\text{SNeIa}} = 0.38 - 0.50$ for Seric 159-03. Werner et al. (2006) obtained a lower value of $f_{\text{SNeIa}} = 0.27 \pm 0.03$ based on a similar analysis of a deep XMM-Newton observation of 2A0335+09. In a recent paper, de Plaa et al. (2007) demonstrated that the derived value of f_{SNeIa} can vary from 0.22 to 0.72 depending on the adopted supernova yields, progenitor metallicity and stellar initial mass function. Our results, together with previous studies, all indicate that the gas surrounding the CDG in clusters has experienced a greater relative enrichment from SNe Ia compared to solar abundance gas.

Since the Fe yield from SNe Ia is almost 10 times greater than the Fe yield from SNcc, the time required to accumulate the observed excess Fe mass can be estimated assuming that only SNe Ia from the CDG are responsible for the enrichment. Scaling the present day SNe Ia rate in early-type galaxies given in Cappellaro et al. (1999), using an average B-R=1.8 for the CDGs in our clusters and our adopted cosmology gives,

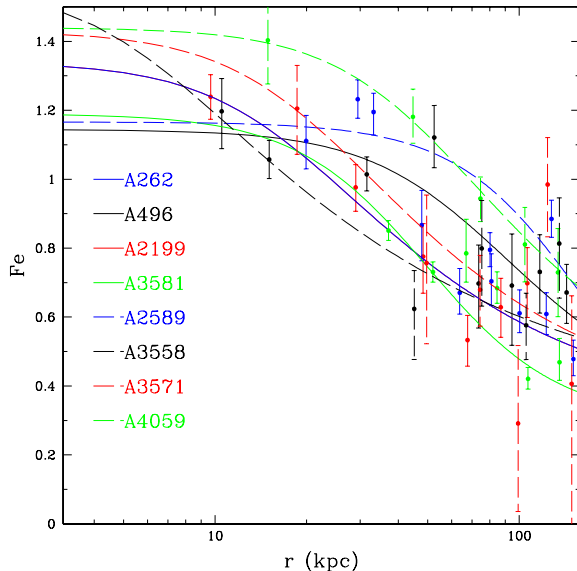


FIG. 4.— Fe abundance (relative to the solar value in Anders & Grevesse 1989) vs. radius for each cluster in our sample. The line types are described in the caption to Fig. 1.

$$R_{\text{SNeIa}} = 1.63 \times 10^{-2} \left(\frac{L_R}{10^{11} L_{\odot R}} \right) \text{yr}^{-1}. \quad (1)$$

TABLE 3
SI MASS WITHIN THE CENTRAL 100 KPC AND INFERRED SNE Ia HEATING RATE

| Name | $M_{Si}(tot)$ (M_{\odot}) | $[Si/Fe]_{tot}$ | τ_0 (Gyr) | τ_e (Gyr) | H_{SNeIa} (erg s^{-1}) | H_{SNeIa}/L_{bol} |
|-------|----------------------------------|------------------|-------------------|-------------------|--|---------------------|
| A262 | $(9.4 \pm 1.5) \times 10^7$ | -0.10 ± 0.07 | 6.7 | 5.4 | 8.7×10^{41} | 0.04 |
| A496 | $(2.7 \pm 0.8) \times 10^8$ | -0.07 ± 0.11 | 7.0 | 5.5 | 2.3×10^{42} | 0.02 |
| A2199 | $(2.0 \pm 0.6) \times 10^8$ | -0.13 ± 0.12 | 5.6 | 4.7 | 2.1×10^{42} | 0.01 |
| A2589 | $(1.1 \pm 0.3) \times 10^8$ | -0.30 ± 0.10 | 8.6 | 6.4 | 1.5×10^{42} | 0.03 |
| A3558 | $(2.0 \pm 0.6) \times 10^8$ | -0.08 ± 0.11 | 2.9 | 2.6 | 3.9×10^{42} | 0.04 |
| A3571 | $(1.8 \pm 0.5) \times 10^8$ | -0.17 ± 0.08 | 2.6 | 2.4 | 4.4×10^{42} | 0.02 |
| A3581 | $(7.7 \pm 0.7) \times 10^7$ | -0.21 ± 0.06 | 6.5 | 5.2 | 8.9×10^{41} | 0.03 |
| A4059 | $(1.7 \pm 0.4) \times 10^8$ | -0.33 ± 0.10 | 7.6 | 5.8 | 2.7×10^{42} | 0.03 |

Notes: Cluster name, total Si mass within the central 100 kpc, ratio of total Si mass to Fe mass relative to the solar ratio within 100 kpc, the time required to produce the presently observed excess Fe mass assuming a constant SNe Ia rate (τ_0) and an evolving SNe Ia rate (τ_e), the SNe Ia heating rate and the SNe Ia heating rate relative to the bolometric X-ray luminosity of the gas. All errors are given at the 1σ confidence level.

The SNe Ia rate for E/S0 galaxies derived by Mannucci et al. (2005) is approximately 20% lower than the rate in Cappellaro et al. (1999), but is within the statistical uncertainties. Table 3 shows the time, τ_0 , required to reproduce the observed excess Fe mass in these clusters using the Fe yield for SNe Ia given above and assuming that R_{SNeIa} is a constant. Accounting for Fe enrichment from SNcc using $f_{SNeIa} = 0.53$, the mean value in our sample, only decreases the required enrichment time by 11%. We also estimate the time required to reproduce the excess Fe mass if $R_{SNeIa} \propto (t/t_H)^{-1}$ (where $t_H = 13.7$ Gyr). This time-dependence is consistent with previous calculations for the evolving rate of SNe Ia (e.g., Loewenstein & Mathews 1987; David, Forman & Jones 1990; Renzini et al. 1993). Table 3 shows that the excess Fe mass within the central 100 kpc in these clusters can be produced by SNe Ia from the CDGs in 3-7 Gyr. These times are lower limits since we do not account for the expulsion of Fe beyond the central 100 kpc or mass deposition.

Assuming that each SNe Ia generates 10^{51} erg, the present day SNe Ia heating rate is only a few percent of the bolometric X-ray luminosity within the central 100 kpc in these clusters (see Table 3). Core collapse supernovae are unlikely to significantly increase the total supernova heating rate since the observed star formation rate in the CDGs in cool-core cluster seldom exceeds $20 M_{\odot} \text{ yr}^{-1}$ (Rafferty et al. 2006). In A262, the star formation rate is constrained to be less than $0.015 M_{\odot} \text{ yr}^{-1}$. Assuming a Salpeter IMF (for which 1 SNcc is produced for every $100 M_{\odot}$ of gas consumed into stars) and a star formation rate of $10 M_{\odot} \text{ yr}^{-1}$, the heating rate from SNcc would be $3.0 \times 10^{42} \text{ erg s}^{-1}$, which would significantly increase the heating rate from SNe Ia alone.

4.1. The Relative Distribution of the Excess Fe

If the Fe produced by SNe Ia remains stationary after being injected into the hot gas and there is no mass deposition, then the ratio of excess Fe mass density to stellar mass density ($\rho_{Fe(ex)}/\rho_*$) should be independent of radius. This prediction is in strong conflict with the observed trend which clearly shows that the excess Fe is significantly more extended than the stellar mass in each cluster (see Fig. 5). The curves in Fig. 5 are calculated using a cubic spline fit to the Fe abundance profiles. Fig. 5 also shows that there is some evidence that the excess Fe

is more centrally concentrated in clusters with shorter cooling times. For comparison, we also show in Fig. 5 the expected values of $\rho_{Fe(ex)}/\rho_*$ if the Fe has accumulated over the past 5 or 7.5 Gyr (using the evolving SNe Ia rate given above) and remained stationary without any mass deposition. While the average values of $\rho_{Fe(ex)}/\rho_*$ within the central 100 kpc are consistent with the expected accumulation of Fe over the past 5-7.5 Gyr, there is clearly a deficit of Fe within the central 30-50 kpc and an excess at larger radii.

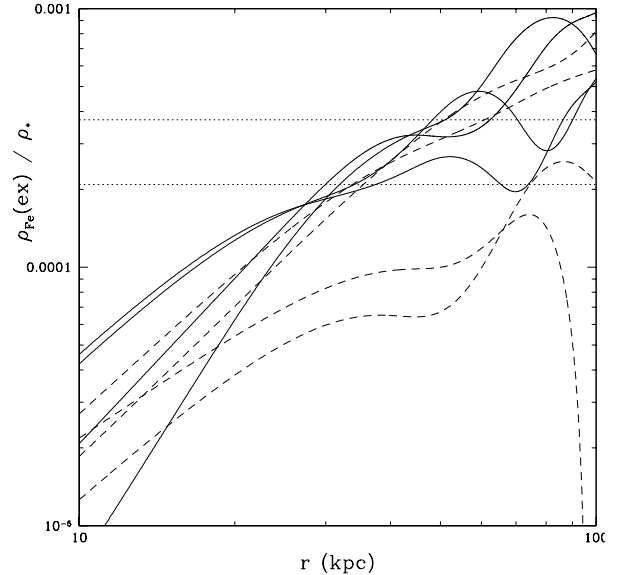


FIG. 5.— Ratio of excess Fe mass density to stellar mass density vs. radius for each cluster in our sample. The line types are described in the caption to Fig. 1. The two horizontal dotted lines indicate the ratio that would result from the accumulation of Fe from SNe Ia over the past 5 (lower line) and 7.5 Gyr (upper line) assuming the Fe remains stationary after being injected and no mass deposition. From top to bottom, the clusters with short cooling times are: A2199, A496, A262 and A3581. From top to bottom, the clusters with long cooling times are: A4059, A3571, A2589 and A3558. The deprojected Fe abundance in A3571 drops slightly below 0.3 solar near 100 kpc which produces a sharp decline in $\rho_{Fe(ex)}/\rho_*$ at this radius.

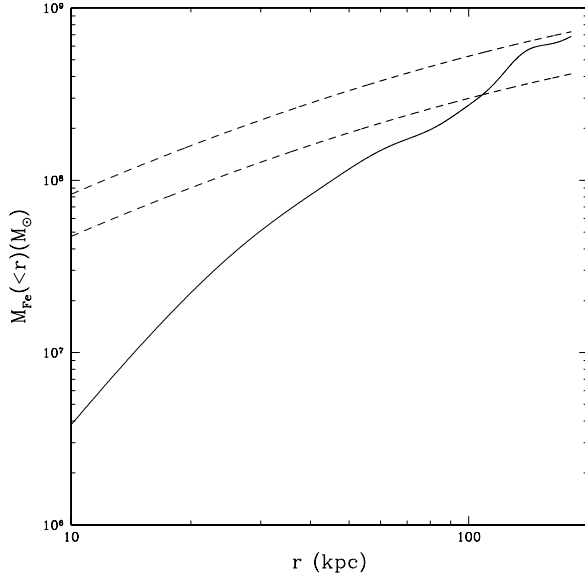


FIG. 6.— Integrated excess Fe mass in A2199 (solid line) compared to predictions based on the accumulation of Fe from SNe Ia over the past 5 (lower dashed line) and 7.5 Gyr (upper dashed line) assuming the Fe remains stationary after being injected and no mass deposition.

5. MECHANISMS FOR PRODUCING AN EXTENDED FE DISTRIBUTION

We explore two possible explanations for the more extended distribution of the excess Fe relative to the stellar mass, including: 1) bulk expansion of the gas due to AGN heating and 2) turbulent diffusion of Fe.

5.1. Bulk Expansion

The integrated excess Fe mass observed in A2199 and the predicted values if the Fe has accumulated from SNe Ia over the past 5 or 7.5 Gyr and remained stationary without mass deposition are shown in Fig. 6. This figure shows that the Fe content of the hot gas within the central 30 kpc is a factor of 10 less than the predicted value. We can estimate how much the excess Fe must have expanded since being injected into the ICM by SNe Ia by comparing the predicted and observed integrated excess Fe masses shown in Fig. 6. For example, assuming that the excess Fe has accumulated from SNe Ia over the past 5 Gyr in A2199 and remained stationary without any mass deposition, there should be $10^8 M_\odot$ of excess Fe within the central 17 kpc. The observed Fe distribution shows that there is $10^8 M_\odot$ of excess Fe within the central 45 kpc, thus the Fe must have undergone a net expansion from 17 kpc to about 45 kpc during this time. This estimate does not include the Fe injected at radii between 17 and 45 kpc while the gas is expanding, and is thus a lower limit on the net expansion.

Using this method, we can compute the minimum net expansion factor as a continuous function of radius for each cluster using the cubic spline fits to the Fe abundance profiles. Fig. 7 shows the required expansion factor $(r_f - r_i)/r_i$, where r_i is the initial radius and r_f is the final (present) radius, as a function of r_i for each cluster. The curve with the largest wiggles in Fig. 7 corresponds to A3571, which has the poorest photon statistics in our sample, and hence, the greatest uncertainties in the Fe abundance. Fig. 7 shows some evidence that the net expansion factor of the excess Fe may be greater in clusters with longer central cooling times.

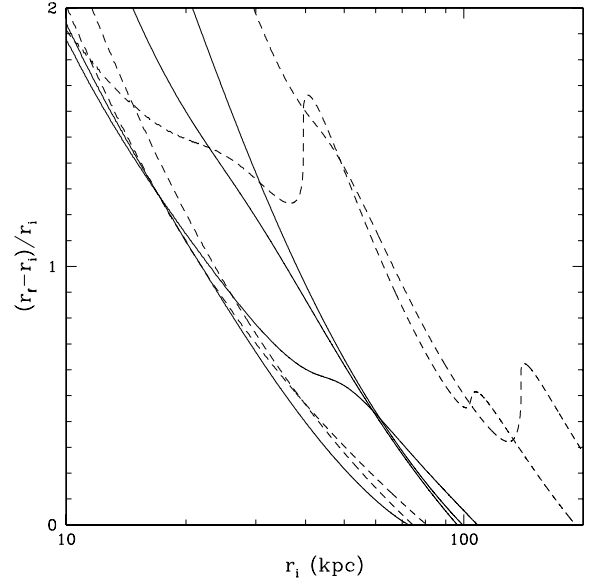


FIG. 7.— The required expansion factor of the gas to reproduce the observed integrated excess Fe mass for all of the clusters in our sample assuming the Fe has accumulated from SNe Ia over the past 5 Gyr and no mass deposition. The line types are described in the caption to Fig. 1.

If we assume that the excess Fe and gas expand together, then the energy required to inflate the gas is:

$$\Delta E = \Delta W + \Delta U \quad (2)$$

where ΔW is the difference in the gravitational potential energy between the final and initial states of the gas and ΔU is the difference in thermal energy. We compute the gravitating mass distribution in each cluster using the deprojected gas density profile shown in Fig. 1, a parametric fit to the deprojected temperature profile based on the functional form used by Allen, Schmidt & Fabian (2001), and the assumption of hydrostatic equilibrium. The potential energy difference for a given mass shell is $\Delta W = \Delta M_{\text{gas}}(r_f)(\phi(r_f) - \phi(r_i))$, where $\Delta M_{\text{gas}}(r_f)$ is the gas mass within a spherical shell centered at radius r_f and ϕ is the gravitational potential. Assuming that the gas is in hydrostatic equilibrium both initially and at present, we show in the Appendix that the change in thermal energy within a given mass shell can be written as:

$$\Delta U = \frac{1}{2}(v_k^2(r_f) - v_k^2(r_i))\Delta M_{\text{gas}}(r_f) \quad (3)$$

where v_k is the Keplerian velocity.

The cumulative total energy difference between the final and initial states of the gas are shown in Fig. 8 for each cluster based on the expansion factors in Fig. 7. We do not include the surface term (i.e., the PdV work done by the expanding gas) in the total energy since, as shown in the Appendix, this term approaches zero at large radii. Fig. 8 shows that $10^{60} - 10^{61}$ erg must have been deposited within the central 100 kpc of these clusters within the past 5 Gyr to inflate the Fe to its present distribution assuming that the Fe and gas expand together. The total potential and thermal energy differences for each cluster within the central 100 kpc are shown in Table 4. This table shows that the potential energy difference accounts for 70-80% of the total energy difference. Our computed energy differences are comparable to the AGN mechanical energy required to evacuate the X-ray cavities and drive the shocks observed in

TABLE 4
ENERGY REQUIREMENTS FOR BULK EXPANSION OF THE GAS

| Name | ΔW (erg) | ΔU (erg) | ΔE (erg) |
|-------|----------------------|----------------------|----------------------|
| A262 | 9.1×10^{59} | 2.1×10^{59} | 1.1×10^{60} |
| A496 | 9.9×10^{59} | 2.2×10^{59} | 1.2×10^{60} |
| A2199 | 2.9×10^{60} | 8.0×10^{59} | 3.7×10^{60} |
| A2589 | 5.8×10^{59} | 3.0×10^{59} | 8.8×10^{59} |
| A3558 | 1.1×10^{61} | 2.1×10^{60} | 1.3×10^{61} |
| A3571 | 1.6×10^{61} | 1.2×10^{60} | 1.7×10^{61} |
| A3581 | 1.0×10^{60} | 2.0×10^{59} | 1.2×10^{60} |
| A4059 | 7.7×10^{59} | 5.9×10^{59} | 1.4×10^{60} |

Notes: Cluster name, increase in potential energy, thermal energy and total energy required to reproduce the observed Fe profiles assuming bulk inflation of the gas within the central 100 kpc.

cool-core clusters (e.g., McNamara et al. 2000, Fabian et al. 2003, Blanton et al. 2003, Nulsen et al. 2005a, Nulsen et al. 2005b; Forman et al. 2005, Wise et al. 2006). The average power required to inflate the gas within the central 100 kpc is $10^{43} - 10^{44} \text{ erg s}^{-1}$, which is also comparable to the mean “cavity power” derived from a sample of cool-core clusters analyzed by Birzan et al. (2004) and Rafferty et al. (2006).

The energy required to reproduce the observed Fe distributions shown in Fig. 8 is a lower limit on the total mechanical energy generated by an AGN, since some of the energy will be radiated away and some of the energy will be deposited beyond 100 kpc. For example, the shock in Hydra A is located 200-300 kpc from the center of the cluster (Nulsen et al. 2005a). Fig. 9 shows the time it will take to dissipate the additional energy required to inflate the gas within a given radius, $t_{\text{loss}} = \Delta E(< r) / L_{\text{bol}}(< r)$. This figure shows that the excess energy within the central 30 kpc of these clusters will be dissipated within $1 - 3 \times 10^8 \text{ yr}$. If AGN outbursts repeat on approximately this timescale, then only the gas within the central 30 kpc will be able to cool and contract before the next AGN outburst, while gas beyond this radius will continuously expand. The gas mass within the central 30 kpc is typically 10% of the total gas mass within the central 100 kpc in these clusters. Thus, if AGN outbursts repeat on timescales of approximately $1 - 3 \times 10^8 \text{ yr}$, then only 10% of the total gas mass within the central 100 kpc is available for further cooling and accretion onto the central supermassive black hole.

5.2. Turbulent Diffusion of Iron

AGN inflated X-ray cavities are commonly found in the centers of cool-core clusters. As these cavities buoyantly rise outward, they will generate turbulent gas motions in their wake. AGN driven shocks expanding into inhomogeneous cluster gas can also generate turbulent gas motions (Heinz et al. 2006) as well as cluster mergers and the motion of the host galaxies in a cluster. Based on the high optical depth toward the center of the Perseus cluster and the lack of any observed resonant scattering in the He-like Fe K_{α} to K_{β} line ratio, Churazov et al. (2004) concluded that there must be significant gas turbulence in the central region of the cluster. Such turbulence will also produce an outward diffusion of Fe as higher abundance gas at small radii is mixed with lower abundance gas at large radii.

We model the outward diffusion of Fe using the same tech-

nique used by Rebusco et al. (2005) and (2006) who estimated the diffusion coefficient, D , and dissipative heating rate in Perseus and 7 other groups and clusters. They performed a series of time-dependent simulations for each cluster with a range of values of D . Each simulation started with a uniform Fe abundance. The excess Fe was assumed to originate from SNe Ia with the same distribution as the stars in the CDG and then diffuse outward. They found that a diffusion coefficient of $D \approx 2 \times 10^{29} \text{ cm}^2 \text{ s}^{-1}$ is required to reproduce the presently observed Fe abundance profiles in these groups and clusters. This method was also used by Graham et al. (2006) to estimate the diffusion coefficient in the Centaurus cluster and determine the characteristics of the turbulence required to locally balance radiative cooling. In addition, Roediger et al. (2007) performed a series of numerical simulations to study the effects of buoyantly rising bubbles on the abundance gradients in cluster atmospheres. They found that the dredging up of low entropy,

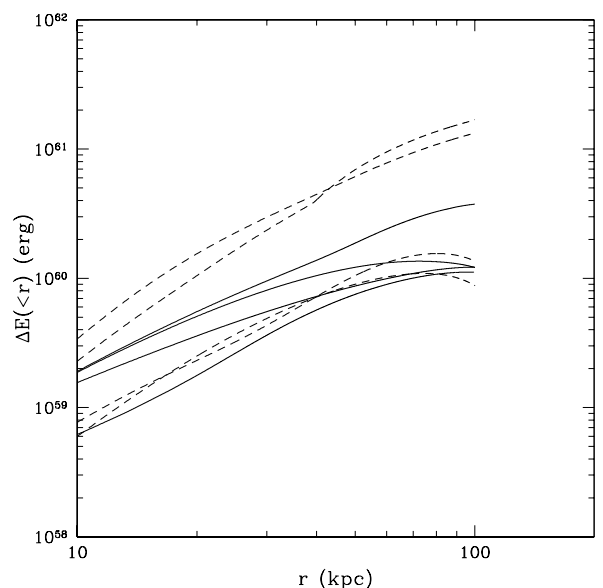


FIG. 8.— The integrated total energy required to inflate the gas and reproduce the observed integrated excess Fe mass distribution in each cluster in our sample assuming the Fe has accumulated from SNe Ia over the past 5 Gyr. The line types are described in the caption to Fig. 1.

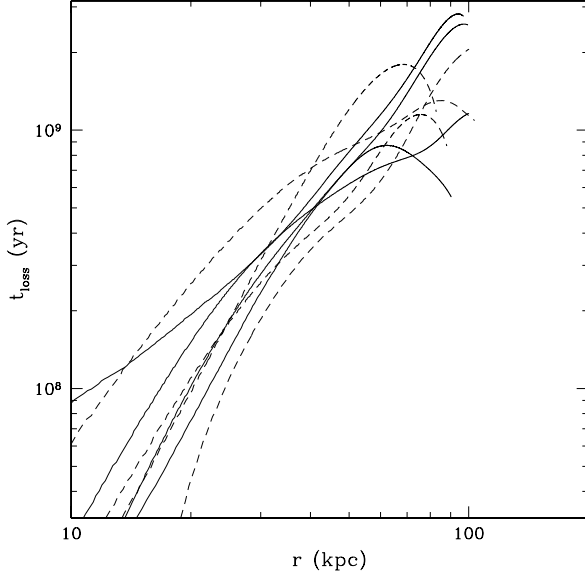


FIG. 9.— The time to dissipate the excess energy shown in Fig. 8 through radiative losses. The line types are described in the caption to Fig. 1.

high abundance gas in the wake of buoyant bubbles can produce effective diffusion coefficients comparable to that required to reproduce the observed Fe abundance profiles in clusters.

Assuming the gas density profile is time-independent, there is no bulk motion of the gas, and isotropic turbulence, the Fe diffusion equation can be written as:

$$\frac{\partial(\rho_g Z_{Fe})}{\partial t} = \vec{\nabla} \cdot (D \rho_g \vec{\nabla} Z_{Fe}) + \dot{\rho}_{Fe, inj} \quad (4)$$

where ρ_g is the gas mass density, Z_{Fe} is the Fe abundance by mass and $\dot{\rho}_{Fe, inj}$ is the Fe mass injection rate per unit volume from SNe Ia. Assuming steady-state (i.e., the outward mass flux of Fe across a given surface is equal to the mass injection rate of Fe within that surface), the diffusion equation can be written as:

$$\int D \rho_g \vec{\nabla} Z_{Fe} \cdot \vec{dA} = -\dot{M}_{Fe}(< R) \quad (5)$$

Fig. 10 shows the required diffusion coefficient to maintain a steady-state Fe abundance profile as a function of radius for each cluster in our sample. For most clusters, the diffusion coefficient decreases outward, attaining a minimum value between 20-50 kpc, and then increases at larger radii. This results from the flattening of the Fe abundance profiles at small and large radii. As the Fe abundance gradient decreases, larger diffusion coefficients are required to transport the Fe outward at the same rate that it is being injected by SNe Ia.

The smallest values of D occur in regions where the Fe abundance profiles are the steepest.

We can determine if the outward diffusion of Fe is primarily driven by particle diffusion or turbulent gas motions by comparing the diffusion coefficient derived above with the particle diffusion coefficient of Fe, given by: $\kappa_{Fe} \approx 1/3 \lambda_{Fe} v_{Fe}$, where λ_{Fe} is the Fe mean free path and v_{Fe} is the thermal Fe velocity. The shortest Fe mean free path is the Fe-proton mean free path. Using the expressions in Spitzer (1962) to compute the Fe-proton mean free path assuming that all Fe is He-like (i.e., an ion charge of 24), we plot the ratio D/κ_{Fe} as a function of

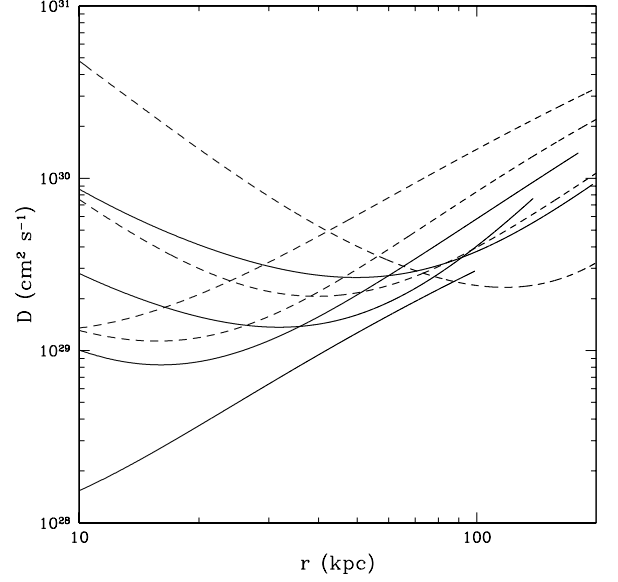


FIG. 10.— The diffusion coefficient, D , required to maintain a steady-state Fe abundance profile in each cluster in our sample. The line types are described in the caption to Fig. 1.

radius for each cluster in Fig. 11. This figure shows that the required rate of Fe diffusion to maintain a steady-state Fe abundance profile is $10^3 - 10^4$ times greater than the particle diffusion rate. Thus, the outward diffusion of Fe must be driven by turbulent gas motions.

5.2.1. General Constraints on Turbulence

The diffusion coefficient can be written as $D = c_1 u l$ (where c_1 is a constant of order unity, l is length scale of the largest eddies and u is turbulent velocity for eddies of size l). Assuming the turbulence can be characterized by a local mixing length

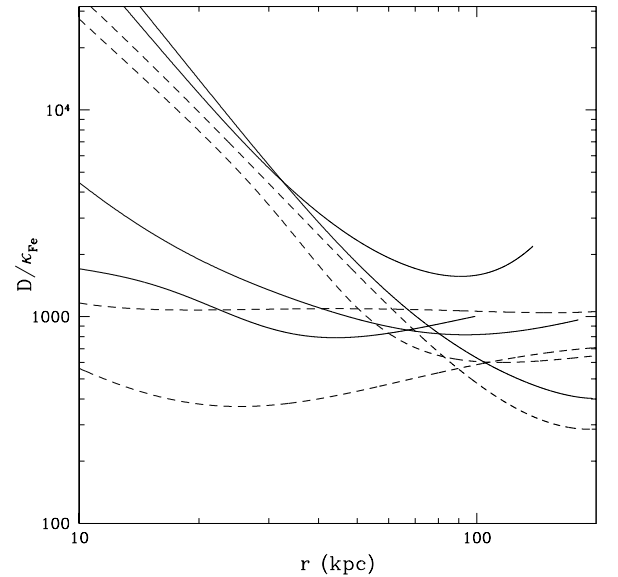


FIG. 11.— The ratio of the diffusion coefficient, D , to particle diffusion coefficient for Fe, $\kappa_{Fe} = l_{Fe} v_{Fe}$, where l_{Fe} is the Fe-proton mean free path and v_{Fe} is the thermal velocity of the Fe ions. This figure shows that the diffusion of Fe is dominated by turbulent gas motions ($D/\kappa_{Fe} \gg 1$) at all radii in each cluster. The line types are described in the caption to Fig. 1.

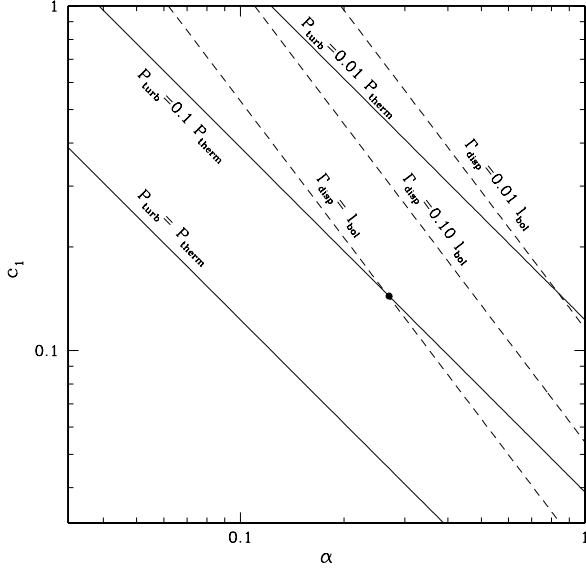


FIG. 12.— The solid lines indicate values of α and c_1 (defined in the text) that produce constant values of $P_{\text{turb}}/P_{\text{therm}}$ using the conditions in A2199 at a radius of 30 kpc. The dashed lines correspond to constant values of $\Gamma_{\text{disp}}/l_{\text{bol}}$. The solid point shows the values of α and c_1 required to completely balance radiative cooling with a turbulent pressure equal to 10% of the thermal pressure at a radius of 30 kpc in A2199.

prescription (see the discussion in Chandran 2005), the size of the largest eddies can be written as $l = \alpha r$, where α is a parameter between 0 and 1 and r is the radial distance from the cluster center. The turbulent eddies will cascade to smaller and smaller scales until the eddy turn over time is comparable to the viscous loss time and the turbulent kinetic energy is dissipated at a rate per unit volume given by:

$$\Gamma_{\text{diss}} = c_2 \rho_g \frac{u^3}{l} \quad (6)$$

where c_2 is a constant of order unity. This equation can be written as:

$$\Gamma_{\text{diss}} = \left(\frac{c_2}{c_1^3 \alpha^4} \right) \frac{\rho_g D^3}{r^4} \quad (7)$$

Written in this form, Γ_{diss} is much more sensitive to c_1 and α compared to c_2 and we therefore set $c_2 = 0.42$ based on the discussion in Dennis & Chandran (2005).

We can place some general constraints on c_1 and α based on the inferred turbulent gas pressure and energy dissipation rate. Based on recent work by Mahdavi et al. (2007) and Churazov et al. (2007), gravitating masses within the cores of rich clusters computed from X-ray data assuming only thermal pressure support are typically within 10% of the masses derived from optical data and weak lensing. This indicates that the sum of turbulent gas pressure, non-thermal gas pressure and magnetic pressure must be less than about 10% of the thermal gas pressure in cluster cores. The turbulent gas pressure can be written as:

$$P_{\text{turb}} = \left(\frac{1}{c_1 \alpha} \right)^2 \frac{\rho_g D^2}{3r^2} \quad (8)$$

Using the gas properties in A2199 at a radius of 30 kpc and the diffusion coefficient required to maintain a steady-state Fe

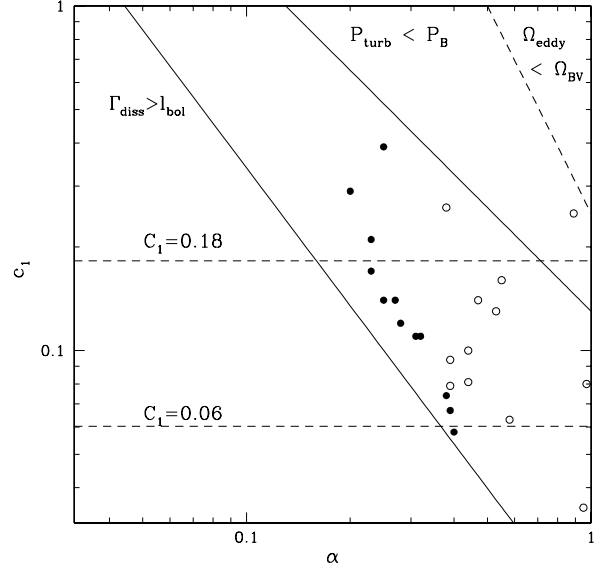


FIG. 13.— The solid points give the values of α and c_1 (defined in the text) required to balance radiative cooling with heating by turbulent dissipation with a turbulent pressure equal to 10% of the thermal pressure at radii of 30, 50 and 70 kpc in clusters with short cooling times. The open points are the corresponding points for clusters with long cooling times. The horizontal dashed lines bracket possible values of c_1 from the literature. Values of α and c_1 in the lower left corner of the figure can be excluded since these values produce heating by turbulent dissipation that exceeds radiative cooling at all radii in all clusters. Values of α and c_1 in the upper right hand corner of the figure can also be excluded since these values produce turbulent pressures less than the magnetic pressure (assuming $P_B = 0.01 P_{\text{therm}}$). Values of α and c_1 in the extreme upper right hand corner of the figure yield eddy frequencies less than the Brunt-Vaisala frequency.

abundance profile, we plot lines of constant $P_{\text{turb}}/P_{\text{therm}}$ in the c_1 and α parameter space in Fig. 12. Also shown in Fig. 12 are lines of constant $\Gamma_{\text{diss}}/l_{\text{bol}}$, where l_{bol} is the X-ray bolometric luminosity per unit volume at the same location in A2199. This figure shows that there is only a narrow strip in α and c_1 parameter space where the dissipation of turbulent gas motions is energetically important (i.e., $0.1 l_{\text{bol}} < \Gamma_{\text{disp}} < l_{\text{bol}}$) and dynamically unimportant (i.e., $P_{\text{turb}} < 0.1 P_{\text{therm}}$). This figure also shows that the dissipation of small turbulent eddies ($\alpha \lesssim 0.1$) can only balance radiative losses if c_1 is of order unity, while the dissipation of large eddies can balance radiative losses with a much broader range of c_1 .

We have computed the values of α and c_1 required to balance radiative cooling through the dissipation of turbulence with $P_{\text{turb}} = 0.1 P_{\text{therm}}$ at radii of 30, 50 and 70 kpc in each cluster. The resulting data points are shown in Fig. 13. This figure shows that most of the clusters require eddies with $\alpha = 0.2 - 0.5$ and that there is a trend that clusters with shorter cooling times require smaller eddies to suppress radiative cooling. There are certain regions in the c_1 and α parameter space that can be excluded. The region in the lower left corner of Fig. 13 indicates regions where the dissipation of turbulence with $P_{\text{turb}} = 0.1 P_{\text{therm}}$ exceeds the bolometric X-ray luminosity in all clusters at all radii. The region in the extreme upper right of Fig. 13 can be excluded due to the effects of buoyancy. Buoyancy suppresses turbulent diffusion if the Brunt-Vaisala frequency, given by:

$$\omega_{\text{BV}}^2 = \frac{g}{\gamma} \frac{d(\ln P / \rho^\gamma)}{dr} \quad (9)$$

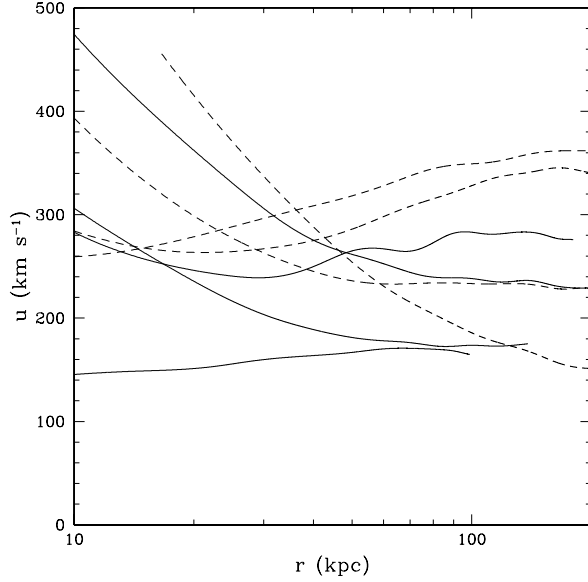


FIG. 14.— The turbulent velocity, u , required to balance radiative cooling with heating by turbulent dissipation for each cluster in our sample. The line types are described in the caption to Fig. 1.

where γ is the ratio of specific heats and g is the acceleration of gravity, is greater than the eddy turnover frequency, $\omega_{\text{eddy}} = u/l = D/(c_1 \alpha^2 r^2)$. The region to the right of the heavy dashed line in Fig. 13 can be excluded since these values of α and c_1 produce eddy turnover frequencies less than the Brunt-Vaisala frequency in all clusters at all radii. Turbulent diffusion is also suppressed when $P_{\text{turb}} < P_B$, where P_B is the magnetic pressure. Assuming $P_B = 0.01 P_{\text{therm}}$ (which roughly corresponds to a magnetic field strength of $B = 3 - 5 \mu\text{G}$ in the center of these clusters), a larger region in the upper right corner of the Fig. 13 can be excluded. These calculations show that the suppression of turbulent diffusion by buoyancy is only significant for very low values of B . Based on a review of the literature by Dennis & Chandran (2005), they find a range of estimates on c_1 from 0.06 to 0.18. These values are shown at horizontal dashed lines in Fig. 13. Our calculations show that the region in the α and c_1 parameter space required for turbulent diffusion and dissipation to play a key role in clusters of galaxies is mostly consistent with all of these constraints.

5.2.2. Balancing Cooling Through Turbulent Dissipation

In this section, we derive the properties of the turbulence required to locally balance radiative losses at all radii in each cluster using the diffusion coefficient necessary to maintain a steady-state Fe abundance profile. Substituting $l = D/c_1 u$ into eq. (7) gives $\Gamma_{\text{diss}} = c_1 c_2 \rho_g u^4 / D$. By setting $\Gamma_{\text{diss}} = f l_{\text{bol}}$ with $c_1 = 0.11$, $c_2 = 0.42$ and $f = 1$, the turbulent velocity required to balance radiative cooling can be determined (see Fig. 14). This figure shows that turbulent gas motions with $u = 150 - 300 \text{ km s}^{-1}$ are required to locally balance radiative cooling in these clusters. Even though this calculation assumes that turbulent dissipation completely balances radiative losses, the estimated turbulent velocities are very insensitive to the fraction of the cooling balanced by dissipation since $u \sim (f l_{\text{bol}})^{1/4}$. For example, if turbulent dissipation only balances 10% of the radiative losses, then the resulting velocities would only be reduced by a factor of 2 below the values shown in Fig. 14.

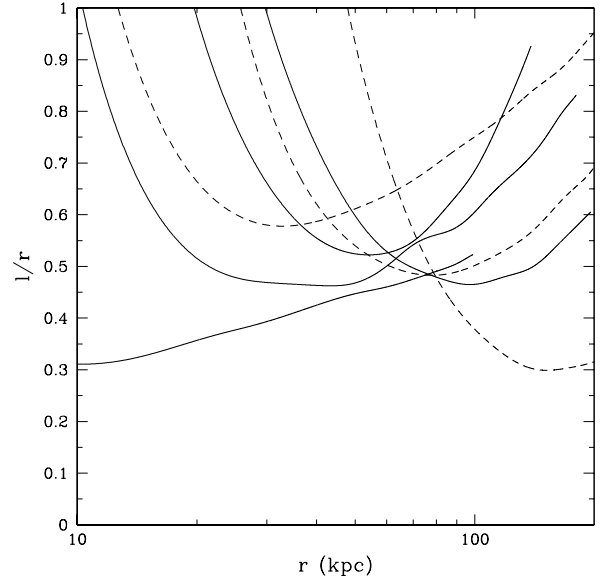


FIG. 15.— The ratio of the length scale of the largest eddies to the cluster radius as a function of cluster radius for each cluster. The line types are described in the caption to Fig. 1.

We can also estimate the scale length of the largest eddies from $l = D/(c_1 u)$, which can be written as:

$$l = \left(\frac{D}{c_1} \right)^{3/4} \left(\frac{c_2 \rho_g}{f l_{\text{bol}}} \right)^{1/4} \quad (10)$$

Using the same values for c_1 and c_2 as given above, and $f = 1$, we have computed the ratio l/r as a function of radius for each cluster (see Fig. 15). It is apparent from this figure that large eddies with $\alpha > 0.5$ are required to locally balance radiative losses and maintain a steady-state Fe abundance profile. There are regions in Fig. 15 with $l/r > 1$, which are clearly unphysical. Eq. (10) shows that the estimated eddy size is the most sensitive to c_1 and is fairly insensitive to c_2 and f . Increasing c_1 to 0.18 (within the possible range noted by Dennis & Chandran 2005) would yield $l/r < 1$ in all clusters at all radii. The ratio of the turbulent pressure to the thermal pressure is shown in Fig. 16 using the turbulent velocities shown in Fig. 14. This figure shows that $P_{\text{turb}}/P_{\text{therm}} < 0.1$ at most radii, indicating that turbulent gas pressure is of little consequence in estimating the gravitating masses of clusters even in cases when turbulent dissipation completely compensates for radiative cooling.

5.2.3. Balancing Cooling Through Turbulent Diffusion of Entropy

Since the entropy increases outward in all of the clusters in our sample (i.e., the gas is convectively stable), the outward diffusion of Fe will lead to an inward diffusion of entropy producing a heating rate per unit volume given by:

$$\Gamma_{\text{diff}} = \vec{\nabla} \cdot (D \rho_g T \vec{\nabla} S) \quad (11)$$

Using the diffusion coefficient required to maintain a steady-state Fe abundance profile, the ratio $\Gamma_{\text{diff}}/l_{\text{bol}}$ is shown as a function of radius for each cluster in Fig. 17. In some regions (e.g., the central region in A496), the divergence term in eq. (11) is negative and turbulent diffusion locally cools the gas. Fig. 17 shows that the inward diffusion of entropy is an important heating mechanism in cluster cores. In half of the clusters

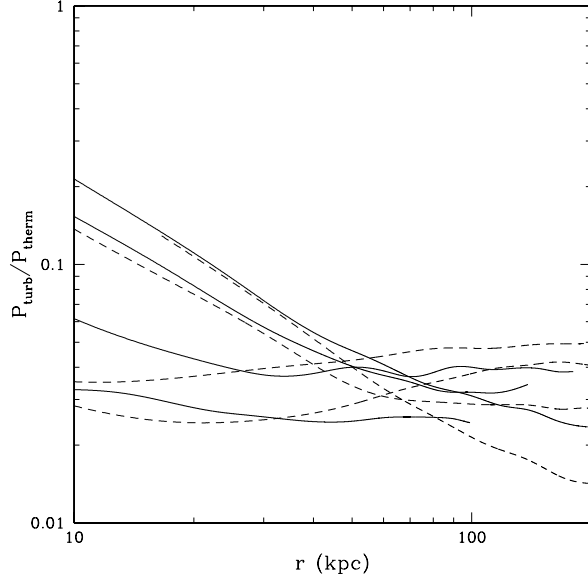


FIG. 16.— The ratio of turbulent gas pressure using the velocities in Fig. 14 to the thermal gas pressure. The line types are described in the caption to Fig. 1.

with long cooling times (A3558 and A3571), turbulent diffusion is sufficient to balance radiative losses at all radii and no additional heating from turbulent dissipation is required. In all other clusters, some additional heating by turbulent dissipation is required. The required values of Γ_{diss}/l_{bol} are shown in Fig. 17 in regions where $\Gamma_{diff}/l_{bol} < 1$. The turbulent velocities necessary to balance cooling through a combination of turbulent dissipation and diffusion are shown in Fig. 18. These velocities are not significantly different than those shown in Fig. 14 which assumed that turbulent dissipation alone balances radiative losses. In A496 and A3581, which have central regions with $\Gamma_{diff} < 0$ (see Fig. 17), larger velocities are required to balance cooling compared to the velocities shown in Fig. 14.

6. DISCUSSION AND CONCLUSIONS

Based on a systematic analysis of 8 clusters of galaxies, we find that the excess Fe in the centers of these clusters is significantly more extended than the stellar distribution in the CDG. There is a slight trend that the central Fe excess is more extended in clusters with the long cooling times compared to clusters with short cooling times. The most likely origin for the excess Fe in cluster cores is enrichment by SNe Ia from the CDG. Using the SNe Ia rate in early-type galaxies from Cappellaro et al. (1999), the total excess Fe mass within the central 100 kpc in these clusters can be produced by SNe Ia in 3-7 Gyr. We have not included the effects of ram pressure stripping of host galaxies in our calculations. Based on a series of numerical simulations of clusters, Schindler et al. (2005) found that ram pressure stripping of host galaxies only increases the central Fe abundance by 0.07-0.10 (relative to the solar value). Most of the clusters in our sample have central Fe abundances approaching the solar value, so ram pressure stripping should not be a significant factor. Domainko et al. (2006) also performed numerical simulations of the effects of ram pressure stripping on the enrichment of the intracluster medium in three cluster models and found that the metallicity of the gas within the central 1.3 Mpc was only enriched by 10%. The ratio of total Si to

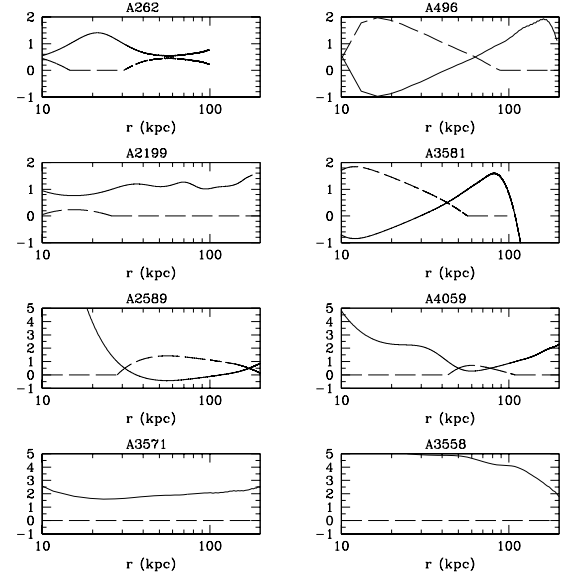


FIG. 17.— The ratio of the heating rate by turbulent diffusion of entropy per unit volume to the bolometric X-ray per unit volume (Γ_{diff}/l_{bol} - solid line) as a function of radius for each cluster in our sample. Also shown is the ratio of the heating rate by turbulent dissipation per unit volume to the bolometric X-ray luminosity per unit volume (Γ_{diss}/l_{bol} - dashed line) in regions where turbulent diffusion alone is insufficient to locally balance cooling. The top 4 clusters have central cooling times less than 1 Gyr while the bottom 4 clusters have longer cooling times.

Fe mass within the central 100 kpc in these clusters gives an average SNe Ia fraction of $f_{SNeIa} = 0.53$, which is approximately twice the solar ratio. Using the SNe Ia rate in Cappellaro et al. and $f_{SNeIa} = 0.53$, the total (Type Ia and core collapse) supernova heating rate is, at most, 3-8% of the bolometric X-ray luminosity within the central 100 kpc in these clusters.

In the absence of any heating mechanism, the excess Fe in the central regions of clusters should have the same distribution as the stars in the CDG, however there is ample evidence from

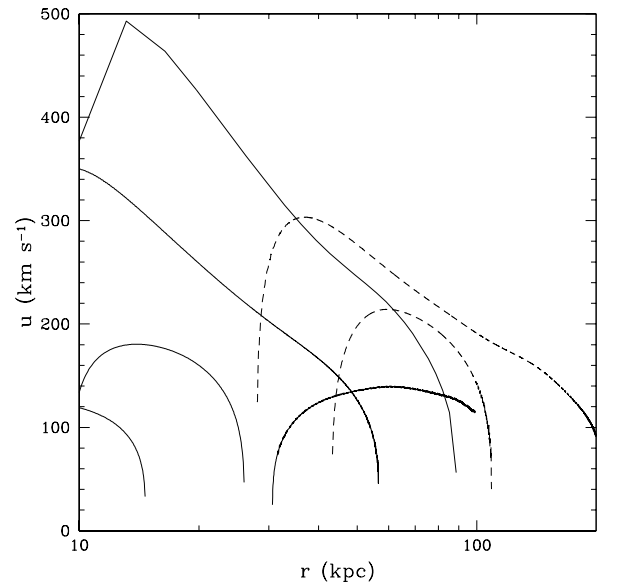


FIG. 18.— The turbulent velocity, u , required to balance radiative cooling with a combination of heating by turbulent diffusion of entropy and dissipation for all of the clusters in our sample. The line types are described in the caption to Fig. 1.

Chandra and XMM-Newton observations that AGN mechanical heating has a significant impact on the energetics of the gas in the central regions of clusters. Estimates on the total mechanical energy deposited into the gas from past AGN outbursts can be obtained from the presently observed Fe distribution. We find that the excess Fe must have undergone significant inflation since being injected by SNe Ia, with $(r_f - r_i)/r_i \approx 1$ within the central 30-50 kpc, to reproduce the present Fe distribution in these clusters. Using the observed gas temperature and density distributions, along with the assumption of hydrostatic equilibrium, we determined the gravitating mass distribution in each cluster and the potential energy difference between the present and initial excess Fe distributions. Assuming that the Fe and gas expand together, we find that a total energy (thermal plus potential) of $10^{60} - 10^{61}$ erg must have been deposited into the central 100 kpc in these clusters. Since the required enrichment time for the excess Fe is approximately 5 Gyr, this gives an average mechanical power of $10^{43} - 10^{44}$ erg s⁻¹ over this time. This power is comparable to the “cavity power” computed by Birzan et al. (2004) and Rafferty et al. (2006) for a sample of cool-core clusters.

The greater extent of the excess Fe in clusters compared to the stars in the CDG could also arise from turbulent diffusion without a significant expansion of the total gas mass. Chandra and XMM-Newton observations have shown that AGNs in the centers of clusters have a dramatic impact on the morphology and energetics of the hot gas (see the review by McNamara & Nulsen 2007). Nuclear outbursts can heat the gas through hydrodynamic shocks, the dissipation of sound waves and through the inflation and subsequent evolution of buoyant bubbles. The energy required to inflate a bubble is simply the PdV work required to inflate the bubble plus the internal energy of the material within the bubble, i.e., the enthalpy of the bubble. Churazov et al. (2002) showed that the bubble enthalpy is transferred to the hot gas via drag as the bubble buoyantly rises outward. This energy initially takes the form of turbulent gas kinetic energy in the wake of the rising bubble. The exact evolution of buoyant bubbles depends on the whether the bubbles are filled with hot gas or relativistic particles (Sijacki et al. 2008). Heating by the dissipation of turbulent kinetic energy in clusters has been studied by Cho et al. (2003), Kim & Narayan (2003), Voigt & Fabian (2004), Dennis & Chandran (2005), Chandran (2005), but only Rebusco et al. (2005) and (2006) used the observed Fe distribution in clusters to constrain the properties of the turbulence. Since all of the clusters in our sample have a positive entropy gradient, the outward diffusion of Fe will also lead to an inward diffusion of entropy and further heating of the central gas.

We have obtained some general constraints on turbulence in cluster cores by noting that the turbulent gas pressure must be less than 10% of the thermal gas pressure (to give agreement between cluster masses derived from X-ray data assuming only thermal pressure support and optical and weak lensing mass measurements), the turbulent gas pressure must be greater than the magnetic pressure (to prevent significant suppression of turbulent diffusion) and the eddy turn over frequency must be greater than the Brunt-Vaisala frequency. These considerations show that there is only a narrow strip in c_1 and α parameter space (where $D = c_1 ul$ and $l = \alpha r$) where turbulence can play a significant role in the gas energetics in clusters without violating one of these constraints. We also find that small eddies (small values of α) can only be energetically important if c_1 is

close to unity, while larger eddies must have smaller values of c_1 to be energetically important without also being dynamically important.

We find that a diffusion coefficient of $10^{29} - 10^{30}$ cm² s⁻¹ is required to maintain a steady-state Fe abundance profile (i.e., the outward mass flux of Fe across a given surface is equal to the mass injection rate of Fe from SNe Ia within that surface) in our sample of 8 clusters. These values are comparable with those derived by Rebusco et al. (2005) and (2006) based on a comparison between a set of time-dependent models for the Fe enrichment in clusters and the presently observed Fe distributions. The particle diffusion coefficient of Fe is approximately $\kappa_{Fe} \approx 1/3 \lambda_{Fe} v_{Fe}$, where λ_{Fe} is the Fe-proton mean free path and v_{Fe} is the thermal Fe velocity. In these clusters, the particle diffusion coefficient of Fe is typically 10^{-3} times the diffusion coefficient estimated assuming a steady-state Fe abundance profile. This shows that particle diffusion by itself is incapable of maintaining a steady-state Fe abundance profile and that the outward diffusion of Fe must be driven by turbulence. The dissipation of turbulent kinetic energy can be an important heating mechanism in the centers of clusters. If the characteristic velocity of the turbulence is approximately 150 - 300 km s⁻¹, then the dissipation of turbulent kinetic energy can completely balance radiative cooling in these clusters. Rebusco et al. (2005) and (2006) derived similar turbulent velocities for their sample of 8 groups and clusters. Even if the velocity of the turbulence is sufficient to completely balance radiative cooling, we find that the resulting turbulent gas pressure is less than 10% of the thermal gas pressure at most radii in these clusters.

In addition to heating by turbulent dissipation, we find that heating by turbulent diffusion of entropy is also an important heating mechanism in cluster cores. Radiative cooling can be completely balanced by turbulent diffusion alone in 2 out of the 4 clusters in our sample with central cooling times longer than 1 Gyr. All of the other clusters in our sample require some additional heating by turbulent dissipation to fully balance cooling. Dennis & Chandran (2005) calculated the significance of turbulent diffusion, turbulent dissipation and heat conduction in three cool-core clusters assuming the turbulence in clusters is generated by cosmic rays produced by the central supermassive black hole that mix with the thermal gas. They parameterized the length scale of the largest eddies as $l = l_0 + \alpha r$ and generated a set of models with different values of α for each cluster. In their models with $\alpha > 0.5$, they found that heating by turbulent diffusion is the dominant heating mechanism, while in models with $\alpha < 0.5$, heating by turbulent dissipation dominates. This is easily understood since heating by turbulent diffusion is directly proportional to D , and hence l (see eq. 11), while heating by turbulent dissipation is inversely proportional to l (see eq. 6), with all other parameters held fixed. We directly calculate l at each radius in each cluster by assuming that the Fe abundance profiles are in steady-state and that radiative losses are balanced through a combination of turbulent dissipation and diffusion. In general, we find $\alpha > 0.5$ at most radii in most clusters which increases the significance of heating by turbulent diffusion.

In the above discussion, we assumed that clusters are in steady-state. While this is a reasonable assumption for examining clusters on timescales longer than the time between AGN outbursts, it is possible that the level of turbulence in clusters is periodic and peaks shortly after an AGN outburst. Deep Chandra observations of several clusters have detected a series of

X-ray cavities emanating from the central AGN. If turbulence is driven by the dredging up of low entropy, enriched gas behind a buoyant AGN inflated bubble (along with the subsequent infall of higher entropy, less enriched gas), then the initial heating triggered by an AGN outburst is due to the turbulent diffusion of entropy. Hydrodynamic isotropic Kolmogorov turbulence cascades according to $u \sim l^{1/3}$. Heating by turbulent diffusion scales as $\Gamma_{diff} \sim ul \sim l^{4/3}$, while heating by turbulent dissipation scales as $\Gamma_{diff} \sim u^3/l \sim l^0$. Thus, heating by turbulent

diffusion decreases as the turbulence cascades to smaller scales while heating by turbulent dissipation remains a constant. However, both the break up of turbulent eddies to smaller scales and the dissipation of turbulence occur on approximately an eddy-turn over time, so both processes essentially operate together.

This work was supported in part by NASA grant GO7-8127X. PEJN also acknowledges NASA grant NAS8-01130. The authors would also like to thank the anonymous referee for many useful suggestions and comments.

REFERENCES

- Allen, S., Schmidt, R. & Fabian, A. 2001, MNRAS, 328, L37.
 Anders, E. & Grevesse, N. 1989, Geo. Cosmo. Acta, 53, 197.
 Arnaud, M. et al. 2002, A&A, 390, 27.
 Baldi, A., Etti, S., Mazzotta, P., Tozzi, P. & Borgani, S. 2007, Bell, E. & de Jong, R. 2001, ApJ, 550, 212.
 Best, P., Kaiser, C., Heckman, T. & Kauffmann, G. 2006, MNRAS, 368, 67.
 Blanton, E., Sarazin, C. & McNamara 2003, ApJ, 585, 227.
 Binney, J. & Tremaine, S. 1987, in Galactic Dynamics, (Princeton University Press: Princeton).
 Birzan, L., Rafferty, D., McNamara, B., Wise, M., Nulsen, P. 2004, ApJ, 607, 800.
 Bohringer, H., Matsushita, K., Churazov, E., Finoguenov, A. & Ikebe, Y. 2004, A&A, 416, L21.
 Cappellaro, E., Evans, R. & Turatto, M. 1999, A&A, 351, 459.
 Chandran, B. 2005, ApJ, 632, 809.
 Cho, J., Lazarian, A., Honein, A., Knaepen, B., Kassinos, S. & Moin, P. 2003, ApJ, 589, L77.
 Churazov, E., Sunyaev, R., Forman, W. & Bhringer, H. 2002, MNRAS, 332, 729.
 Churazov, E., Forman, W., Jones, C., Sunyaev, R. & Bhringer, H. 2004, MNRAS, 347, 29.
 Churazov, E., Forman, W., Vikhlinin, A., Tremaine, S., Gerhard, O. & Jones, C. 2007 (astro-ph 0711.4686).
 David, L., Forman, W. & Jones, C. 1990, ApJ, 359, 29.
 David, L., Jones, C. & Forman, W. 1995, ApJ, 445, 578.
 David, L., Nulsen, P., McNamara, B., Forman, W., Jones, C., Ponman, T., Robertson, B., Wise, M. 2001, ApJ, 557, 546.
 De Grandi, S., Etti, S., Longhetti, M. & Molendi, S. 2004, A&A, 419, 7.
 Dennis, T. & Chandran, D. 2005, ApJ, 622, 205.
 de Plaa, J., Werner, N., Bykov, A., Kaastra, J., Mendez, M., Vink, J., Bleeker, J., Bonamente, M. & Peterson, J. 2006, A&A, 452, 397.
 de Plaa, J., Werner, N., Bleeker, J., Vink, J., Kaastra, J. & Mendez, M. 2007, A&A, 465, 345.
 Domainko, W., Mair, M., Kapferer, W., van Kampen, E., Kronberger, T., Schindler, S., Kimeswenger, S., Ruffert, M. & Mangete, O. 2006, A&A, 452, 795.
 Dunn, R. & Fabian A. 2006, MNRAS, 373, 959.
 Dunn, R. & Fabian A. 2008, MNRAS, 385, 757.
 Fabian, A., Sanders, J., Allen, S., Crawford, C., Iwasawa, K., Johnstone, R., Schmidt, W. & Taylor G. 2003, MNRAS, 344, 43.
 Finoguenov, A., David, L. & Ponman, T. 2000, ApJ, 544, 203.
 Finoguenov, A., Arnaud, M. & David, L. 2001, ApJ, 555, 191.
 Finoguenov, A. & Jones, C. 2002, ApJ, 574, 754.
 Forman, W., Nulsen, P., Heinz, S., Owen, F., Eilek, J., Vikhlinin, A., Markevitch, M., Kraft, R., Churazov, E., Jones C. 2005, ApJ, 635, 894.
 Fukazawa, Y., Makishima, K., Tamura, T., Nakazawa, K., Ezawa, H., Ikebe, Y., Kikuchi, K. & Ohashi, T. 2000, MNRAS, 313, 21.
 Gonzalez, A., Zabludoff, A. & Zaritsky, D. 2005, ApJ, 618, 195.
 Graham, J., Fabian, C., Sanders, J. & Morris, R. 2006, MNRAS, 368, 1369.
 Graham, A., Lauer, T., Colless, M. & Postman, M. 1996, ApJ, 465, 534.
 Grevesse, N. & Sauval, A. 1998, Sp. Sci. Rev., 85, 161.
 Heinz, S., Bruggen, M., Young, A. & Levesque, E. 2006, MNRAS, 373, 65.
 Iwamoto, K., Brachwitz, F., Nomoto, K., Kishimoto, N., Umeda, H., Hix, W., Thielemann, F. 1999, ApJS, 125, 439.
 Jones, C. & Forman, W. 1999, ApJ, 511, 65.
 Kim, W. & Narayan, R. 2003, ApJ, 596, L139.
 Kraft, R., Vazquez, S., Forman, W., Jones, C., Murray, S., Hardcastle, M., Worrall, D. & Churazov, E. 2003, ApJ, 592, 129.
 Lauer, T. & Postman, M. 1994, ApJ, 425, 418.
 Lloyd-Davies, E., Ponman, T. & Cannon, D. 2000, MNRAS, 315, 689.
 Loewenstein, M. & Mathews, W. 1987, ApJ, 319, 614.
 Loewenstein, M. 2006, ApJ, 648, 230.
 Mahdavi, A., Hoekstra, H., Babul, A. & Henry, J. 2007 (astro-ph 0710.4132).
 Mannucci, F., Della Valle, M., Panagia, N., Cappellaro, E., Cresci, G., Maiolino, R., Petrosian, A. & Turatto, M. 2005, A&A, 433, 807.
 Marty, P. et al. 2002, Proc. SPIE, 4851, 208.
 Matteucci, F. 2007 (astro-ph 0704.0770).
 Mazzotta, P., Edge, A. & Markevitch, M. 2003, ApJ, 596, 190.
 McNamara, B. et al. 2000, ApJ, 534, 135.
 McNamara, B. & Nulsen, P. 2007, ARA&A, 45, 117.
 Nulsen, P., McNamara, B., Wise, M. & David, L. 2005a, ApJ, 628, 629.
 Nulsen, P., Hambrick, D., McNamara, B., Rafferty, D., Birzan, L., Wise, M., David, L. 2005b, ApJ, 625, 9.
 Peterson, J., Kahn, S., Paerels, F., Kaastra, J., Tamura, T., Bleeker, J., Ferrigno, C. & Jernigan, J. 2003, ApJ, 590, 207.
 Rafferty, D., McNamara, B., Nulsen, P. & Wise, M. 2006, ApJ, 652, 216.
 Read, A. & Ponman, T. 2003, A&A, 409, 395.
 Rebusco, P., Churazov, E., Bohringer, H. & Forman, W. 2005, MNRAS, 359, 1041.
 Rebusco, P., Churazov, E., Bohringer, H. & Forman, W. 2006, MNRAS, 372, 1840.
 Renzini, A., Ciotti, L., D'Ercole, A. & Pellegrini, S. 1993, ApJ, 419, 52.
 Roediger, E., Bruggen, M., Rebusco, P., Bohringer, H. & Churazov, E. 2007, MNRAS, 375, 15.
 Schindler, S., Kapferer, W., Domainko, W., Mair, M., van Kampen, E., Kronberger, T., Kimeswenger, S., Ruffert, M., Mangete, O. & Breitschwerdt, D. 2005, A&A, 435, L25.
 Schlegel, D., Finkbeiner, D. & Davis, M. 1998, ApJ, 500, 525.
 Sijacki, D., Pfrommer, C., Springel, V. & Enßlin, T. 2008 (astro-ph 0801.3285).
 Spitzer, L. 1962, Physics of Fully Ionized Gases, (Princeton University Press: Princeton).
 Tamura, T., Kaastra, J., den Herder, J., Bleeker, J. & Peterson, J. 2004, A&A, 420, 135.
 Thielemann, F., Nomoto, K. & Hashimoto, M. 1993, in Origin and Evolution of the Elements, eds. Prantzos, N., Vangoni-Flam, E. (Cambridge University Press: Cambridge).
 Tornatore, L., Borgani, S., Matteucci, F., Recchi, S. & Tozzi, P. 2004, MNRAS, 344, L19.
 Tsujimoto, T., Nomoto, K., Yoshii, Y., Hashimoto, M., Yanagida, S., Thielemann, F. 1995, MNRAS, 277, 945.
 Vikhlinin, A., Markevitch, M., Murray, S., Jones, C., Forman, W., Van Speybroeck, L. 2005, ApJ, 628, 655.
 Voigt, L. & Fabian, A. 2004, MNRAS, 347, 1130.
 Wise, M., McNamara, B., Nulsen, P., Houck, J. & David, L. 2007, ApJ, 659, 1153.
 Werner, N., de Plaa, J., Kaastra, J., Vink, J., Bleeker, J., Tamura, T., Peterson, J. & Verbunt, F. 2006, A&A, 449, 475.

APPENDIX

CHANGE IN THERMAL ENERGY OF THE GAS DURING BULK EXPANSION

Assume that the gas initially fills a volume V_i with a radius of R_i . After a period of bulk expansion, the gas fills a final volume of V_f with a radius of R_f . The difference in thermal energy between the final and initial states is simply:

$$\Delta U = \frac{3}{2} \left[\int_0^{V_f} P_f(r_f) dV - \int_0^{V_i} P_i(r_i) dV \right] \quad (1)$$

where P_i is the initial pressure of the gas and P_f is the final gas pressure. Assuming the gas is in hydrostatic equilibrium before and after the bulk expansion, then the pressure is given by:

$$P(r) = \int_r^\infty \rho(r) g(r) dr. \quad (2)$$

where $\rho(r)$ is the gas density and $g(r)$ is the acceleration of gravity. Using eq. (2) in the first integral on the right hand side of eq. (2) gives:

$$\int_0^{V_f} P_f(r_f) dV = \int_0^{V_f} dV \int_{r_f}^\infty \rho_f(r) g(r) dr. \quad (3)$$

Integration by parts gives:

$$\int_0^{V_f} P_f(r_f) dV = \left[V \int_{r_f}^\infty \rho_f(r) g(r) dr \right]_0^{V_f} + \int_0^{V_f} V(r_f) \rho_f(r_f) g(r_f) dr_f \quad (4)$$

which becomes:

$$\int_0^{V_f} P_f(r) dV = \frac{4\pi}{3} \left[R_f^3 \int_{R_f}^\infty \rho_f(r) g(r) dr + \int_0^{R_f} r_f^3 \rho_f(r_f) g(r_f) dr_f \right]. \quad (5)$$

$$= V_f P_f(R_f) + \frac{4\pi}{3} \int_0^{R_f} r_f^3 \rho_f(r_f) g(r_f) dr_f. \quad (6)$$

Using $dM_f = 4\pi \rho_f(r_f) r_f^2 dr_f$ and $v_k^2(r_f) = g(r_f) r_f$, where v_k is the Keplerian velocity, eq. (5) becomes:

$$\int_0^{V_f} P_f(r) dV = V_f P_f(R_f) + \frac{1}{3} \int_0^{M_f} v_k^2(r_f) dM_f. \quad (7)$$

Performing the same calculation for the second term on the right hand side of eq. (1) and taking the difference gives:

$$\Delta U = \frac{3}{2} [V_f P_f(R_f) - V_i P_i(R_i)] + \frac{1}{2} \left[\int_0^{M_f} v_k^2(r_f) dM_f - \int_0^{M_i} v_k^2(r_i) dM_i \right]. \quad (8)$$

Since $M_f = M_i$, this becomes:

$$\Delta U = \frac{3}{2} [V_f P_f(R_f) - V_i P_i(R_i)] + \frac{1}{2} \int_0^{M_f} (v_k^2(r_f) - v_k^2(r_i)) dM_f. \quad (9)$$

At large radii, $r_f - r_i \rightarrow 0$, and the first term converges to zero.